

Dispersive modeling of breaking waves on a slope

Jihwan Kim^a, Geir K. Pedersen^a, Finn Løvholt^{a,b}, Randall J. LeVeque^c

^a*University of Oslo, Department of Mathematics, Oslo, Norway*

^b*Norwegian Geotechnical Institute, Oslo, Norway*

^c*University of Washington, Department of Applied Mathematics, Seattle, USA*

Abstract

The nonlinear shallow water model is widely used in the study of tsunami propagations where the wave dispersion is ignorable. If the wave dispersion becomes important, Boussinesq-type models are often used. In this work, an operational Boussinesq solver, *BoussClaw*, is introduced for modeling fully nonlinear dispersive tsunami propagation, taking into account inundation. In the BOUSSCLAW model, Boussinesq equations from the literatures, based on the depth-averaged velocity and with enhanced dispersion properties, are implemented with a hybrid of the finite volume and finite difference methods. In order to validate BOUSSCLAW, numerical results are compared to the analytical solutions and laboratory experiments. Furthermore, the wave steepening and breaking motion is explored with the help of the full potential boundary integral model.

Keywords:

1. Introduction

Tsunamis are often considered as long waves compared to the water depth, and depth-averaged wave models are consequently widely used in the study of their propagation and inundation. Through the use of numerical shock capturing techniques for modeling the nearshore bore formation of the tsunami, *nonlinear shallow water* (NLSW) models have become the standard model for modeling tsunami propagation and run-up, see e.g. Titov and Synolakis (1995); Imamura (1996); Harig et al. (2008); Berger et al. (2011). Well known applications include

inundation modeling of the recent major tsunami events such as the 2004 Indian
 10 Ocean tsunami (Borrero et al., 2006; Kaiser et al., 2011) and the 2011 Tohoku
 tsunami (Hooper et al., 2013; Romano et al., 2014).

The NLSW models do not incorporate frequency dispersion and are valid
 only for large wavelength-to-depth-ratios ($\lambda/h > 20$). The accumulated effect of
 the frequency dispersion for the wave propagation over the open sea is a function
 15 of propagation time and the shape of the disturbance Glimsdal et al. (2013),
 and may become important for some tsunamis, in particular for landslide sources
 Løvholt et al. (2015). Dispersion may further be of importance, in combination
 with non-linear effects, for the evolution of undular bores Behrens and Dias
 (2015). *Boussinesq-type models* that allow for more accurate modeling of shorter
 20 waves, may be used to model dispersive tsunamis. In the last decades we have
 seen a development on long wave expansions and their numerical formulations.
 New Boussinesq type formulations, such as those introduced by Madsen and
 Sørensen (1992), and Nwogu (1993), displayed improved accuracy, as well as
 extended validity ranges in comparison to the standard formulation of Peregrine
 25 (1967).

In their original formulation, Boussinesq-type models do not take into ac-
 count the post-breaking motion. In order to combine breaking with the Boussinesq-
 type equations several strategies have therefore been suggested. For instance,
 Peregrine (1967) used $A/h = 0.6$ as the break threshold, while pointing out
 30 that this value could reach around 2 in laboratory experiments. Another way
 of incorporating the breaking that was suggested by Kennedy et al. (2000) in-
 cluded diffusive terms in the momentum equation to smear out sharp fronts.
 Løvholt et al. (2013) similarly employed a diffusive model including transport
 terms, but pointed out that breaking wave Boussinesq models were prone to
 35 instabilities. Schäffer et al. (1993) introduced the concept of the *surface roller*.
 Lynett (2006) investigated η_t/c , η_x , $u_{sxx}H^2/c$, and u_s/c , where $c = \sqrt{gH}$ and
 u_s = free surface speed, and then identified that the critical front slope (η_x) is
 the least sensitive breaking threshold. Tissier et al. (2012) suggested a breaking
 decision model based on the surface roller, the maximal front angle and the

40 Froude number. An alternative non-linear diffusive ad-hoc breaking term was suggested Matsuyama et al. (2007), based on their large scale experiments of the wave propagation of undular bores on various slope angles.

Recent developments of operational Boussinesq models, have made use of more sophisticated hybrid numerical techniques such as use of approximate
45 Riemann solvers combined with TVD limiters for the conserved variables, and finite differences for additional higher order terms (Erduran et al., 2005; Kim et al., 2009; Shi et al., 2012), leading among others to the popular FUNWAVE-TVD and COULWAVE-TVD applications. For instance in Shi et al. (2012), Boussinesq terms are switched off the near-shore region where large amplitude-
50 to-depth-ratios occur, implying that only NLSW terms remain in the shallowest region. This allows for a relatively robust treatment of the modeling of the post breaking phase. To this end, the $A/h = 0.8$ threshold suggested by (Shi et al., 2012) based on the Froude similarity analysis by Tonelli and Petti (2009), have in many ways become the standard for incorporating breaking in a feasible and
55 practical way.

In this paper, we present a new hybrid Boussinesq type model BOUSSCLAW, of similar mould as FUNWAVE-TVD and COULWAVE-TVD. The emphasis is twofold. First, to present a careful validation of the model, both towards laboratory experiments and more general reference models. Second, we use the
60 new model in comparison with a full potential reference model to explore how accurate the Boussinesq models can represent the wave evolution until the point of breaking. In the present example, we are finally able to demonstrate that Boussinesq models may be employed to accurately model the near shore tsunami propagation beyond the standard $A/h = 0.8$ threshold depth. Conversely, we
65 find that the use of the standard $A/h = 0.8$ threshold depth invokes a too early formation of a breaking bore. This points out that that the breaking criteria employed so far lacks generality.

This paper is organized as follows: In Section 2, the base model for the wave equations is given and the numerical scheme is outlined, including a von
70 Neuman stability analysis. Section 3 compares results from the BOUSSCLAW

with the analytic solutions and laboratory experiments. Section 4 discusses the wave steepening and using a Boundary Integral Method (BIM) for solving the full potential equations. In Section 5, we compare these results of pre-breaking evolution with Boussinesq type models.

75 2. Model Description

Boussinesq-type equations include non-hydrostatic pressure in an approximate way treat short waves more accurately than the shallow water equations. The Boussinesq-type wave models have been derived by retaining $\mathcal{O}(\epsilon)$ and $\mathcal{O}(\mu)$ terms, where ϵ and μ denote the ratio of wave amplitude to depth and the ratio
80 of depth to wavelength respectively. Various models have been suggested, and the papers of Peregrine (1967), Madsen and Sørensen (1992), Nwogu (1993), Lynett et al. (2002), and Wei and Kirby (1995) are representative examples.

In this work, a new numerical model, called BOUSSCLAW, is introduced. It is an extension of GEOCLAW Clawpack Development Team (2016), and solves the
85 Boussinesq-type equations derived by Schäffer et al. (1993). The BOUSSCLAW model is a hybrid of the finite volume and finite difference solvers with the operation splitting technique. The GEOCLAW software is a part of CLAWPACK Clawpack Development Team (2016) by LeVeque (1997), George (2008) and Berger et al. (2011) which is designed to solve the nonlinear shallow water
90 equations.

2.1. BOUSSCLAW - a new long wave model for tsunami propagation and run-up

2.1.1. Boussinesq-type equations

Schäffer et al. (1993) derived Boussinesq-type equations with an addition of a Padé approximation of the linear dispersion relation. The equations read

$$H_t + (Hu)_x = 0, \tag{1}$$

$$(1 - D)[(Hu)_t] + \left(Hu^2 + \frac{g}{2}H^2\right)_x - gHh_x - Bgh^2(h\eta_x)_{xx} = 0, \tag{2}$$

where the operator D is defined as

$$D(w) = \left(B + \frac{1}{2}\right) h^2 w_{xx} - \frac{1}{6} h^3 \left(\frac{w}{h}\right)_{xx}, \quad (3)$$

for any $w(x, t)$. In the above equations $H(x, t)$ and $u(x, t)$ are the total flow depth and the depth averaged velocity of the water, respectively, $h(x)$ is the still
95 water depth, $\eta(x, t)$ is the surface elevation, and thus $H(x, t) = h(x) + \eta(x, t)$. Moreover, g is the acceleration of gravity, and B is a dispersion parameter. Madsen and Sørensen (1992) has chosen the parameter $B = 1/15$ from a Padé expansion of the linear dispersion analysis. When $B = 0$, this set of the Boussinesq-type equations approximately reduces to that of Peregrine (1967) as the lin-
100 ear dispersion relations are identical. However, unlike Peregrine's momentum equation the hydrostatic parts of (2) are written in a conservative form. This difference will be observed in the numerical procedure and is further elaborated in Appendix A.

The BOUSSCLAW model solves the Boussinesq-type equations (1) and (2)
105 numerically with a hybrid combination of the finite volume and finite difference methods that will be explained in a moment. There have been several studies on this type of hybrid schemes. For example, see Tissier et al. (2011), Shi et al. (2012) and Dutykh et al. (2013).

To facilitate a fractional step method, as outlined below, we move the hydrostatic terms of (2) inside the $(1 - D)$ operator, while balancing with extra terms in the Ψ , to obtain

$$(1 - D)[(Hu)_t + \left(Hu^2 + \frac{g}{2}H^2\right)_x - gHh_x] = -\Psi(x, t), \quad (4)$$

where

$$\begin{aligned} \Psi(x, t) = & \left(B + \frac{1}{2}\right) h^2 ((Hu^2)_x + gH\eta_x)_{xx} \\ & - \frac{1}{6} h^3 \left(\frac{(Hu^2)_x + gH\eta_x}{h}\right)_{xx} - Bgh^2 (h\eta_x)_{xx}. \end{aligned} \quad (5)$$

2.1.2. Numerical scheme

The equations (1) and (4) are written in a form that conserves momentum to leading order in μ , but with the Ψ term as a pseudo source. Such equations

may be solved by a *fractional step method* as described in LeVeque (2002), for instance. First, it is observed that (4) may be formally rewritten as

$$(Hu)_t = - \left\{ \left(Hu^2 + \frac{g}{2} H^2 \right)_x - g H h_x \right\} - (1 - D)^{-1} \Psi(x, t), \quad (6)$$

110 At the first stage of the hybrid scheme, we integrate Hu over a time step taking into account all hydrostatic terms, namely those within the braces on the right hand side, and omitting the source terms involving Ψ . When this is combined with the continuity equation (1) this simply corresponds to advancing the shallow water equations one time step forward. To this end we employ GEOCLAW,
115 a high-order accurate finite volume solver for the shallow water equations with adaptive mesh refinements.

In the second stage, we retain the new H value, but integrate Hu (essentially being the momentum density) further from the first stage by solving

$$(1 - D) [(Hu)_t] = -\Psi. \quad (7)$$

Since the differential operator D contains spatial derivatives, a systems of difference equations must then be solved.

The spatial and time discretization should be carefully chosen for the stability of the second stage. In our numerical scheme, the second order centered
120 scheme is used for the spatial discretization, and a four stage Runge-Kutta method is used for the time integration. The von Neumann stability analysis of this numerical scheme is outlined in Appendix B.

Suppose the spatial domain is divided into n grid cells with the spatial grid size Δx . Arrays of nodal values for flow depth and Hu , respectively, are defined as

$$\mathbf{H} = (H_1, H_2, \dots, H_n)^T, \\ \mathbf{M} = (H_1 u_1, H_2 u_2, \dots, H_n u_n)^T.$$

With time increment Δt the fourth order Runge-Kutta scheme can be written as follows,

$$\mathbf{M}^1 = \mathbf{M}, \quad \mathbf{M}^2 = \mathbf{M} + \frac{\Delta t}{2} \mathbf{S}^1, \quad \mathbf{M}^3 = \mathbf{M} + \frac{\Delta t}{2} \mathbf{S}^2, \quad \mathbf{M}^4 = \mathbf{M} + \Delta t \mathbf{S}^3, \quad (8)$$

where \mathbf{M}^k are intermediate value arrays and \mathbf{S}^k are correpondingly arrays for the time derivatives of Hu , obtained by solving

$$(I - \bar{D})\mathbf{S}^k = -\bar{\Psi}(\mathbf{H}, \mathbf{M}^k), \quad \text{for } k = 1, \dots, 4. \quad (9)$$

Here $\bar{\Psi}$ and \bar{D} represent centered spatial discretizations for the term Ψ and the operator D , respectively. These are given explitley below. Finally the value of \mathbf{M} at the new time level is obtained by

$$\mathbf{M}^+ = \mathbf{M} + \frac{\Delta t}{6} [\mathbf{S}^1 + 2\mathbf{S}^2 + 2\mathbf{S}^3 + \mathbf{S}^4]. \quad (10)$$

In (9), \bar{D} is a tri-diagonal $n \times n$ matrix with elements

$$\bar{D}_{i,i-1} = \frac{1}{\Delta x^2} \left[\left(B + \frac{1}{2} \right) h_i^2 - \frac{1}{6} \frac{h_i^3}{h_{i-1}} \right],$$

$$\bar{D}_{i,i} = \frac{1}{\Delta x^2} \left(-2B - \frac{2}{3} \right) h_i^2,$$

$$\bar{D}_{i,i+1} = \frac{1}{\Delta x^2} \left[\left(B + \frac{1}{2} \right) h_i^2 - \frac{1}{6} \frac{h_i^3}{h_{i+1}} \right].$$

Correspondingly, the i -th element of $\Psi(\bar{\mathbf{H}}, \mathbf{q})$ is

$$\begin{aligned} \bar{\Psi}_i = & \left(B + \frac{1}{2} \right) \frac{h_i^2}{2\Delta x^3} \left[\left(\frac{M_{i+2}^2}{H_{i+2}} - 2\frac{M_{i+1}^2}{H_{i+1}} + 2\frac{M_{i-1}^2}{H_{i-1}} - \frac{M_{i-2}^2}{H_{i-2}} \right) \right. \\ & + g(H_{i+1}(\eta_{i+2} - \eta_i) - 2H_i(\eta_{i+1} - \eta_{i-1}) + H_{i-1}(\eta_i - \eta_{i-2})) \left. \right] \\ & - \frac{1}{6} \frac{h_i^3}{2\Delta x^3} \left[\frac{M_{i+2}^2/H_{i+2} - M_i^2/H_i}{H_{i+1}} - 2\frac{M_{i+1}^2/H_{i+1} - M_{i-1}^2/H_{i-1}}{h_i} \right. \\ & + \frac{M_i^2/H_i - M_{i-2}^2/H_{i-2}}{H_{i-1}} \\ & + g \left(\frac{H_{i+1}(\eta_{i+2} - \eta_i)}{H_{i+1}} - 2\frac{H_i(\eta_{i+1} - \eta_{i-1})}{h_i} + \frac{H_{i-1}(\eta_i - \eta_{i-2})}{H_{i-1}} \right) \left. \right] \\ & - \frac{Bg h_i^2}{2\Delta x^3} (H_{i+1}(\eta_{i+2} - \eta_i) - 2H_i(\eta_{i+1} - \eta_{i-1}) + H_{i-1}(\eta_i - \eta_{i-2})), \end{aligned}$$

for $i = 1, 2, \dots, n$.

125 2.2. Models for comparison

The performance of the Boussinesq model presented here is assessed by comparison with numerical results from a full potential flow model which is described

in Løvholt et al. (2013) and references therein. The model is based on a boundary integral technique and is run with fully nonlinear solitary wave solutions
130 as initial conditions. During shoaling and breaking this model can describe the evolution of a plunger, but breaks down when the plunger reaches the free surface. Hence, the potential flow results are used to determine the point of breaking due to shoaling and to evaluate the evolution of amplitude and wave shape of the current model until this point. Below we refer to the full potential
135 model as the BIM (Boundary Integral Method) model.

Comparison with a pre-existing, fully nonlinear Boussinesq model is facilitated by the application of a Lagrangian model, described in Løvholt et al. (2013). Apart from the use of Lagrangian coordinates the equations employed in this model are similar to (1) and (2). They differ only concerning the non-
140 linearities in the dispersion terms and that the dispersion optimization terms are added in a fully nonlinear fashion. Presently, the Lagrangian model has no established bore capturing facility and is hence valid only to the point of breaking. Results from this model will be referred to as 'Serre', even though the dispersion enhancement is invoked.

145 Results for the Peregrine-type Boussinesq equations are obtained by the GloBouss model. This is a dispersive tsunami propagation model which is based on Peregrine-type equations and discretization on a staggered grid. Further details are found in Løvholt et al. (2008).

For comparison also the version 2.1 of the FUNWAVE-TVD model by Shi
150 et al. (2012) is used. The FUNWAVE-TVD model shares important features with BOUSSCLAW, employing a hybrid of the finite volume and finite difference scheme to solve the fully non-linear higher order dispersive Boussinesq model numerically. While we refer to Shi et al. (2012) for details, we briefly note that FUNWAVE-TVD is based the fully nonlinear Boussinesq equations of Chen
155 (2006). The numerical spatial representation in FUNWAVE-TVD is MUSCL TVD scheme to discretize for the flux and first order terms, whereas a central finite difference scheme Wei et al. (1995) is utilized for the higher order momentum terms. A Runge-Kutta scheme is employed for the time stepping.

3. Numerical Tests

3.1. Solitary wave propagation

In order to validate the numerical approach a solitary wave propagation is tested on a constant water depth. For the initial conditions, the analytic solitary wave solution of the Serre's equations is used since analytic solutions are unknown for the set (1) and (2). Solitary wave solutions to Serre's equations are given as

$$\begin{aligned}\eta(x, t) &= A \operatorname{sech}^2(\kappa(x - ct)), \\ u(x, t) &= c \frac{\eta(x, t)}{h},\end{aligned}\tag{11}$$

where

$$\kappa = \frac{\sqrt{3h}}{2A\sqrt{A+h}}, \quad \text{and} \quad c = \sqrt{g(A+h)}.\tag{12}$$

In this expression, A and h are constants which represent the wave amplitude and the undisturbed water depth respectively.

In Figure 1, snapshots from the BOUSSCLAW's simulation are shown at $t = 0, 4, 8$ and 12 with $\Delta x = 0.1$. For the initial conditions, the solution (11) is used with $A = 0.2$, $h = 1$ and $g = 9.81$. The computational results are in good agreement with the analytic solutions concerning height, shape and propagation speed. The amplitudes decreases very gently as the wave propagates.

The wave energies for the shallow water equations and the Boussinesq equations are E_0 and $E_0 + E_1$, respectively, where

$$E_0 = \frac{1}{2} (g\eta^2 + H\bar{u}^2),\tag{13}$$

$$E_1 = \frac{1}{6} H^3 \bar{u}_x^2 + \frac{1}{2} H^2 h_x \bar{u} \bar{u}_x + \frac{1}{2} H h_x^2 \bar{u}^2.\tag{14}$$

Details are given in (Madsen et al., 1997) and Appendix C.

In Figure 2a, the energy of the solitary wave is shown with $A/h = 0.2$ and $\Delta x = 0.2$. There are fluctuations both in the potential and kinetic energy that is evident when we zoom in, and the total energy decreases showing that the

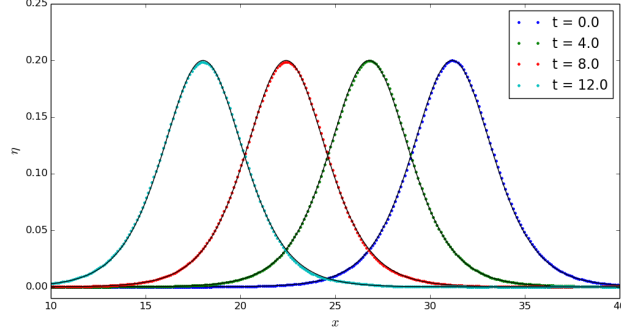


Figure 1: Snapshot of the analytic and computed solitary wave at $t = 0, 4, 8$ and 12 with $A/h = 0.2$. The wave propagates from right to left, and the analytic solutions are black solid lines.

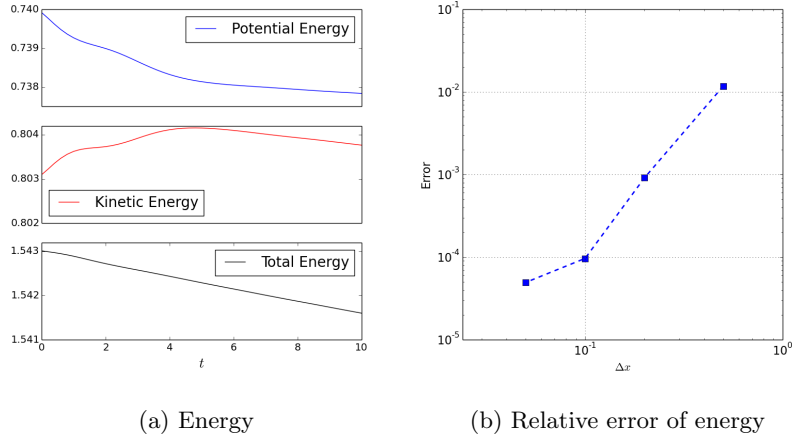


Figure 2: The energy of a solitary wave with $\Delta x = 0.2$ (left), and log-log plot of relative error at $t = 10$ for $\Delta x = 0.05, 0.1, 0.2$ and 0.5 (right).

numerical procedure has dissipation. In Figure 2b, the relative error of the energy at $t = 10$,

$$Error = \frac{|E_{t=0} - E_{t=10}|}{|E_{t=0}|},$$

is shown for different Δx . For a solitary wave on a constant depth, the energy dissipation decreases with the grid increments.

170

3.2. Waves on a composite slope

A physical model was constructed at the Coastal Hydraulic Laboratory of the U.S. Army Corps of Engineers in order to address beach erosion and severe flooding problems Briggs et al. (1995). The model beach consists of three piecewise linear slopes of 1:53, 1:150, and 1:13 with a vertical wall at the shoreline as shown in Figure 3. In the laboratory, the wavemaker was located at 23.23 m. The gauge data from three cases are provided where the ratio A/h is equal to 0.038, 0.259 and 0.681 with $h = 21.8$ cm.

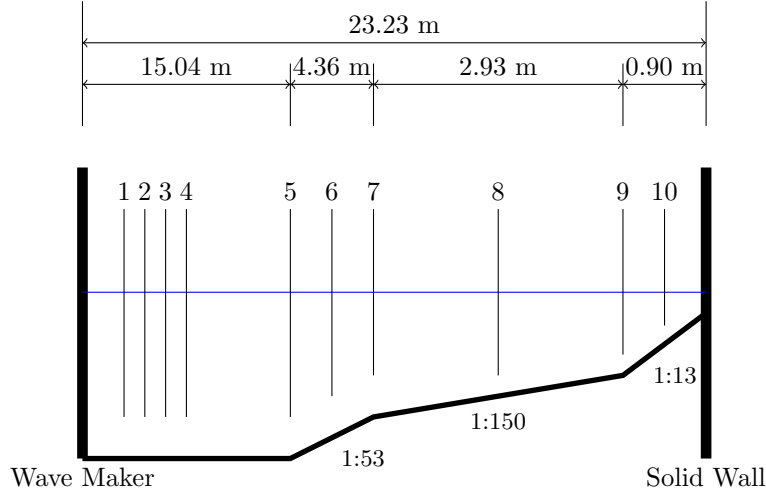


Figure 3: A sketch of the water tank

The second case with $A/h = 0.259$ has been compared with the numerical tests which employed 400 grid points. To specify the incoming wave from the left boundary, the data at Gauge 4 were used for the wave height, and the corresponding velocity (11) was applied.

In Figure 4, water surface elevations at gauges 5, 7 and 8 are shown. The simulated waves are in good agreement with the laboratory measurements. For the reflected waves, larger discrepancies are observed. The increased discrepancy occurs because the full interaction between the wave and the wall at the right boundary is less accurately captured. Friction forces influence the wave evolution along the shallow region near the right wall, but we have not included

these in the present numerical simulation. A better fit may possibly be obtained
 190 by incorporating friction, however, tuning the friction models is not the scope
 of this work.

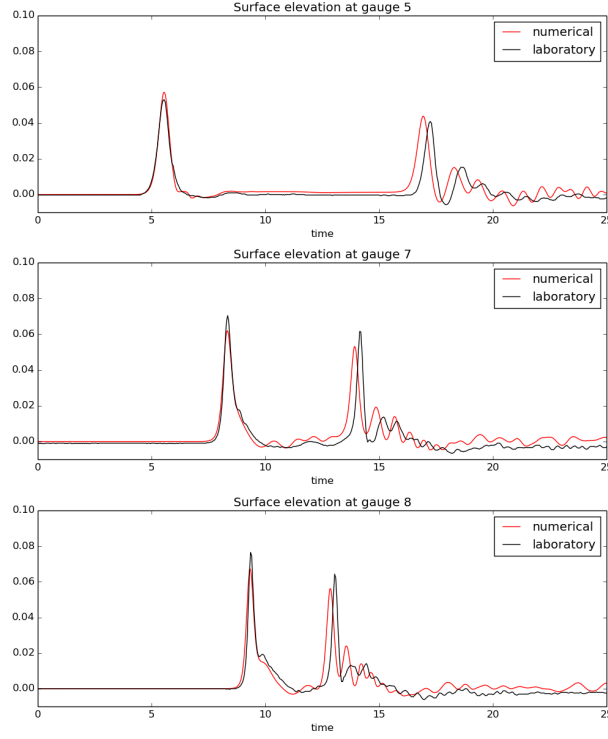


Figure 4: Water surface elevation at gauges 5,7 and 8 for $A/h = 0.269$ case.

4. Simulation of wave steepening and breaking using a BIM model

Synolakis (1987) performed a series of laboratory experiments for the run-
 up of solitary waves on uniform slopes. Here, we are interested in the breaking
 195 cases. One such example in Synolakis (1987) is a solitary wave of amplitude
 $A/h = 0.28$ approaching a slope of 1 : 19.85. In Figure 5, the initial set-up for
 a test is shown.

The set-up of the wave tank in the simulations follows the laboratory experi-
 ments by Synolakis (1987). The bathymetry of the wave tank is composed of a

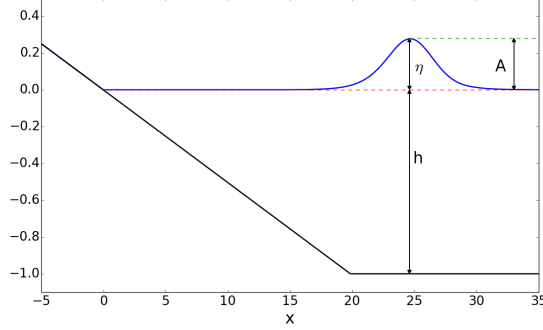


Figure 5: Set-up of a numerical test for Synolakis' experiments.

200 horizontal bottom and a uniform slope as shown in Figure 5. A solitary wave of amplitude $A/h = 0.28$ is generated at the right end of the tank and propagates leftwards to the beach.

We present the results using the non-dimensional time $t^* = t\sqrt{h/g}$ and non-dimensional space $x^* = x/h$. In the following, we drop the asterisks in the presentation of the results. In Synolakis (1987), $t = 0$ was defined as when the wave crest was a distance L from the toe of the slope, where L was given as

$$L = \sqrt{\frac{4A}{3h}} \operatorname{arccosh} \left(\frac{1}{0.05} \right).$$

However, at $t = 0$, the solitary wave has an elevation of 5% of its maximum at the toe of the beach, meaning that the slope has started to interact with the solitary wave. To avoid any such interaction obscuring our analysis, we instead place the
 205 initial solitary wave using equation (11) at $L + 5c$, where c is the shallow water wave celerity. In this way, the initial solitary wave has a negligible interaction with the slope when initialized.

In Figure 6, the laboratory measurements are shown with the computational
 210 results from the BIM model for a breaking wave case of Synolakis with $A/h = 0.28$ and 1 : 19.85 slope at $t = 15$.

Figure 7 shows the numerical results from the BIM model at $t = 17, 18$ and 18.6. In the BIM results a vertical front is observed at $x = 4.02$ and $t = 18.6$ with the maximum wave amplitude $A = 0.414$, and this shows similarity with

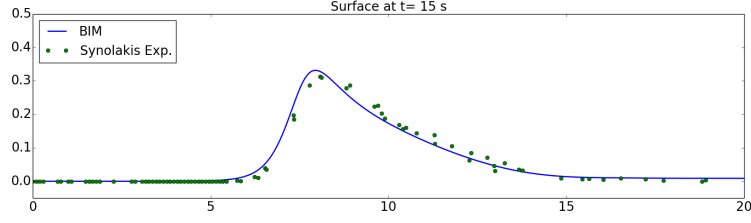


Figure 6: Comparison of the laboratory experiments and BIM at $t=15$ with $A/h = 0.28$ on a slope of 1 : 19.85.

the analysis of Titov and Synolakis (1995) on the wave breaking point. The ratio
of amplitude to depth, A/h , is about 2.01 at the break point. The potential flow
model cannot be run much beyond the breaking points (until attachment of the
plunger only) and gives no information on the following bore propagation. In
Figure 8, computations of the shallow water equations (present model without
the second fractional step) display a premature bore formation which checks the
amplification during the subsequent shoaling. As a consequence the amplitude
in the shallow water equations simulation is markedly smaller than that of the
potential flow model when the latter indicates breaking.

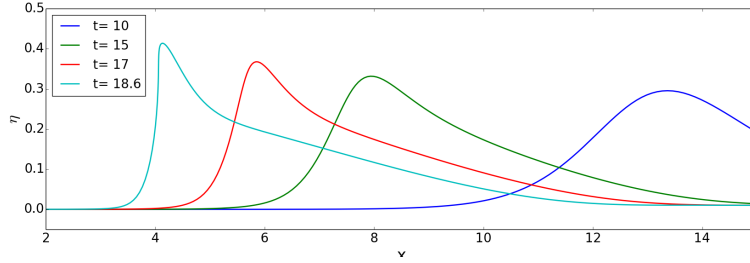


Figure 7: Computational results from BIM of a wave with $A/h = 0.28$ on a slope of 1 : 19.85. A vertical front is observed at $t = 18.6$.

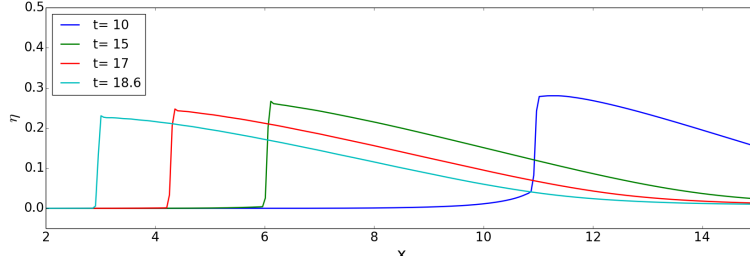


Figure 8: Computational results from SWE at $t = 10, 15, 17$ and 18.6 .

5. Pre-breaking and breaking wave evolution using depth averaged models

225

We use the setup described in section 4 for the Boussinesq modeling of solitary waves on a slope. Figure 9 shows the snapshots of the water surface at $t=16$ and 18.6 from BIM and BOUSSCLAW with $B=0$ and $1/15$. When the wave is smooth at $t=16$, the BOUSSCLAW results are similar. . At the break point, $t = 18.6$, larger differences are observed. If $B = 0$, the wave speed is slightly faster than the BIM result, but the wave amplitude is similar. When $B = 1/15$, the wave speed matches the BIM results better, but the amplitude is slightly smaller. In general, the computational results are rather similar with $B = 0$ and $1/15$.

235 Next, the BOUSSCLAW simulations are compared with those of other Boussinesq solvers, namely FUNWAVE Shi et al. (2012), GLOBOUSS Løvholt et al. (2010) and the Serre type formulation Løvholt et al. (2013). As noted above, the original Serre's equations are enhanced by adding the Schäffer et al. (1993) terms.

240 In Figure 10, snapshots from different numerical models are shown at $t=15$, 17 and 18 . At $t=15$, the computational results from different numerical tools show slightly different results, but the general pattern is similar. At $t=17$, some discrepancies are observed that can be split into two groups, and GLOBOUSS and FUNWAVE are similar while BOUSSCLAW and Serre's results are similar. The
245 wave amplitudes computed by GLOBOUSS and FUNWAVE, are more than 10 %

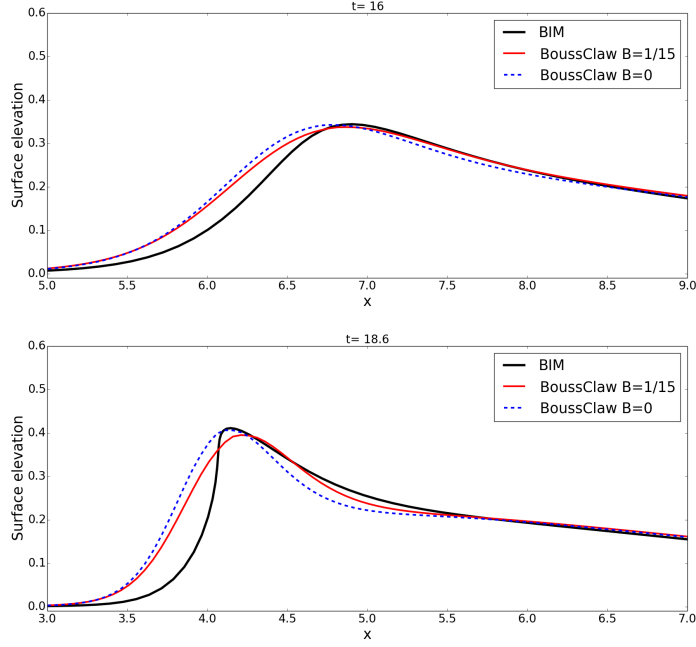


Figure 9: Snapshots of BIM and BOUSSCLAW with $B=0$ and $1/15$ at $t=16$, and 18.6 .

larger than BIM. The wave amplitude continues to increase with GLOBOUSS and FUNWAVE simulations, and the difference from the BIM result becomes larger at $t = 18$. The results from the Serre and BOUSSCLAW models clearly more similar to those of the BIM model. Especially, the wave amplitudes are
250 correctly determined by these models.

5.1. Wave Breaking

In order to catch wave breaking in a heuristic fashion, we may choose to invoke the threshold $\epsilon_B := \eta/h$ for BOUSSCLAW. When the threshold is reached, the wave breaking is supposed to be initiated, and the dispersive terms are
255 suppressed. At the breaking, the set of equations is locally switched to the shallow water equations for the corresponding wave packet, and the trailing waves are solved with the Boussinesq equations if the thresholds are not reached. In the numerical simulation of the BOUSSCLAW model, the ratio ϵ_B reaches the threshold 0.8 at $t = 14.9$ when the peak of the wave is at $x = 8.03227$. In the

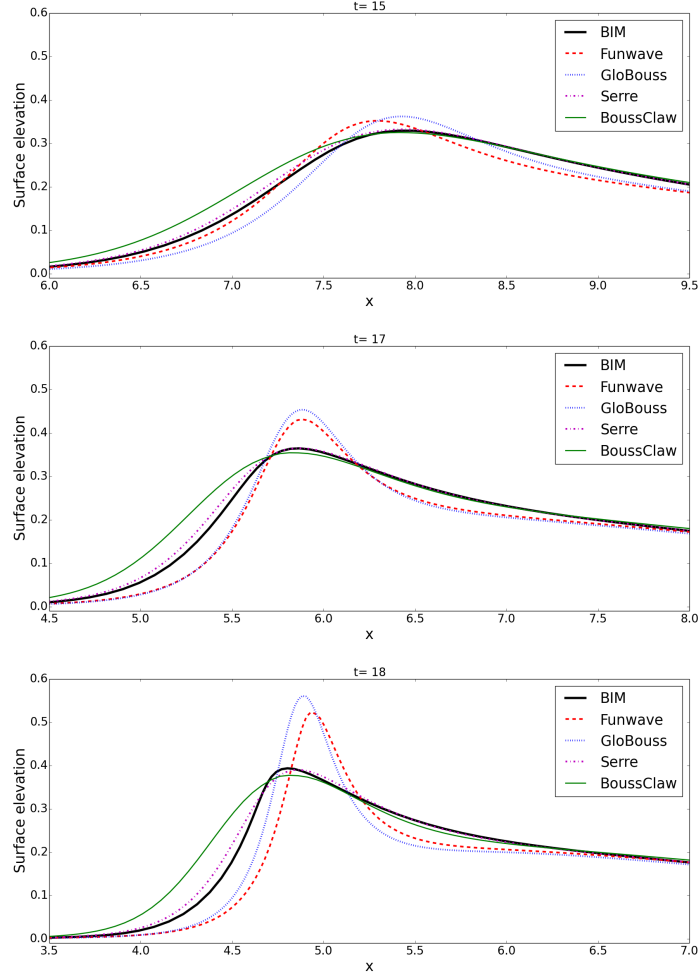


Figure 10: Snapshots of BIM, Serre, GLOBOUSS, BOUSSCLAW and FUNWAVE at $t = 15, 17$ and 18 . The BOUSSCLAW is used with $B=1/15$, and the Peregrine's form is used for GLOBOUSS.

260 following, we explore the wave evolution with and without the application of this threshold.

In Figure 11, snapshots are shown at $t=15, 17$, and 18.6 from BIM, BOUSS-CLAW and SWE. At $t=15$, the difference between BIM and BOUSSCLAW is small, but the difference becomes noticeable in the wave shape and amplitude
265 at $t = 17$ and 18.6 . As the governing equations are switched to the shallow

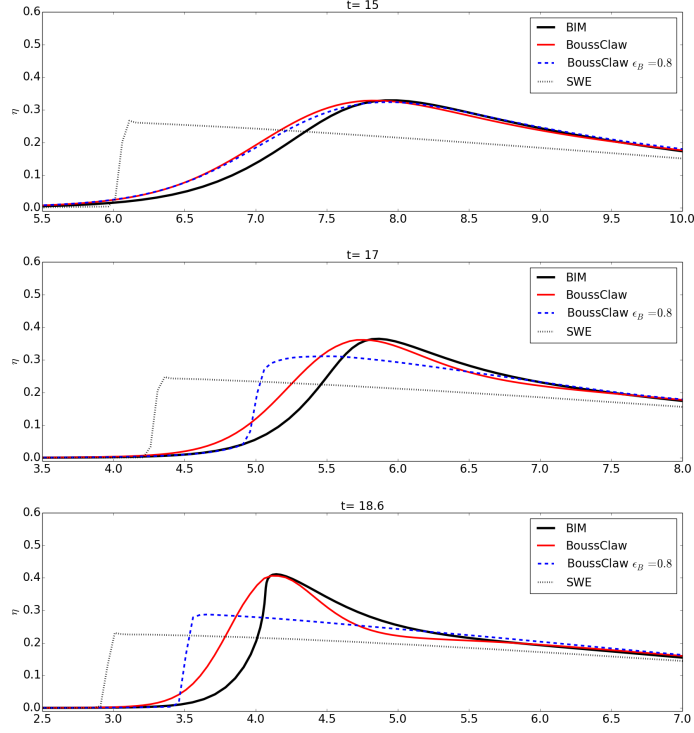


Figure 11: Comparison of BIM, BOUSSCLAW and SWE with $\epsilon_B = 0.8$ at $t=15, 17$ and 18.6 .

water equations, the a bore is forming, and the wave amplitude decreases.

Figure 12 shows the amplitude to depth ratio, ϵ_B , as function of the crest location. With BIM simulations, the wave starts breaking at $x = 4.09$. When the crest in the BOUSSCLAW simulation reaches $x = 4.09$ we find $A/h = 1.97$,
 270 the ratio of wave speed to celerity (u/\sqrt{gH}) is 1.034 and maximum surface slope angle of 39.1° .

5.2. Wave Energy

The wave energy is nearly conserved when the wave is smooth, but decreases as the wave breaks. The wave energy expressions for the shallow water equations and Boussinesq equations are E_0 and $E_0 + E_1$ respectively, which are given in
 275 (13) and (14).

In Figure 13, the wave energy E_0 and $E_0 + E_1$ are shown. The energy

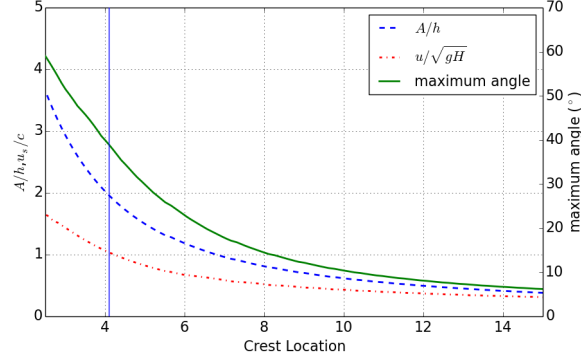


Figure 12: Plot of A/η , u_s/c and maximum angle of waves vs. crest location. BIM shows the wave break at $x = 4.09$.

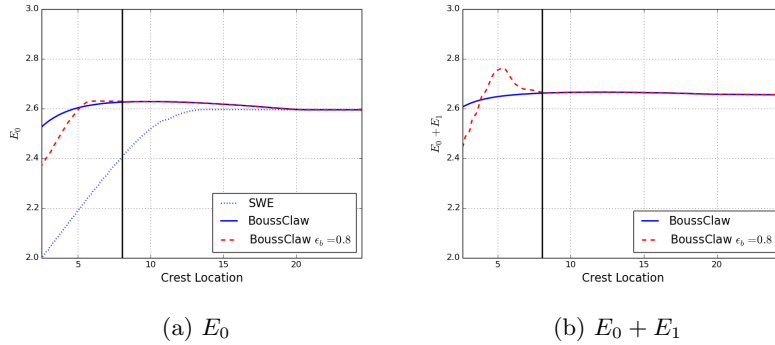


Figure 13: Energy plots of SWE and BOUSSCLAW. The vertical line is at $x = 8.03227$ m where $\epsilon_B = 0.8$, and the governing equations are switched to the SWE from the Boussinesq equations.

denotes the aggregate of the wave energy in the entire computational domain and is shown as function of the crest location. In the left panel, the energy E_0 is well-preserved for the shallow water equations before the wave forms a shock, and then the energy dissipates after a shock is formed. In the right panel, $E_0 + E_1$ is well-preserved for the BOUSSCLAW simulation during deep water propagation, but the value decreases slightly as the wave steepens near the shoreline. When the threshold $\epsilon_B = 0.8$ is used, the energy $E_0 + E_1$ is well-preserved as shown on the right figure before the threshold is reached. When

the crest is located at $x = 8.03227$ with $\epsilon_B = 0.8$, the wave energy E_0 on the left figure does not decrease immediately. The energy E_0 is preserved for a while, then starts to decrease as a shock is formed.

6. Conclusion

290 In the present paper we have presented a new operational Boussinesq type model, BOUSSCLAW, for modeling fully non-linear dispersive tsunami propagation, taking also into account drying-wetting during inundation and withdrawal on the beach. BOUSSCLAW resembles much used operational models such as FUNWAVE-TVD and COULWAVE-TVD, but is based on a slightly simpler and
295 more transparent set of governing equations, and has a slightly different numerical scheme. We have tested numerical implementation towards analytical solitary wave expressions as well as laboratory experiments.

Making use of the experiments of Synolakis (1987) enabled us to constrain a set of different long wave models, including BOUSSCLAW, as well as a full
300 potential BIM reference model. Using the BIM, we were able to explore in detail the post-breaking behaviour, and to identify the point of breaking accurately. This was useful for determining the validity of the respective long wave models. First, we found that by using standard NLSW models, the point of breaking will be located too far offshore. Boussinesq models provide the opportunity
305 of providing a more accurate description of the near shore propagation and shoaling. However, in current practise the Boussinesq terms are often omitted near shore through the $A/h > 0.8$ threshold criteria. As a consequence, the point of breaking may be misinterpreted also in Boussinesq type models.

In the present example, we investigated the near shore propagation over
310 a relatively gentle shelf of $1/19.85$ slope, and in this case the actual onset of breaking occurred for $A/h \approx 2$, which is significantly later than what would be predicted in any standard approach (NLSW or Boussinesq). As demonstrated in this paper, the combined effects of non-linearities and dispersion influence the solution markedly, when accumulated to the point of breaking. It is noted that

315 the artificial effect discovered would depend on the slope, and the $A/h = 0.8$
 limited may well work better on a much gentler slope as it is primarily derived
 based on solitary wave evolution on constant depth. On the other hand, $1/19.85$
 slope is already quite gentle, and the offset between the reference solution and
 Boussinesq models using this criteria may be even more pronounced for steeper
 320 slopes.

References

- H. A. Schäffer, P. A. Madsen, R. Deigaard, A Boussinesq model for waves
 breaking in shallow water, *Coastal Engineering* 20 (3) (1993) 185–202.
- V. V. Titov, C. E. Synolakis, Modeling of breaking and nonbreaking long-wave
 325 evolution and runup using VTCS-2, *Journal of Waterway, Port, Coastal, and
 Ocean Engineering* 121 (6) (1995) 308–316.
- F. Imamura, Long-wave runup models, chapter Simulation of wave-packet prop-
 agation along sloping beach by TUNAMI-code, *World Scientific* 3 (1996) 4.
- S. Harig, Chaeroni, W. S. Pranowo, J. Behrens, Tsunami simulations on several
 330 scales, *Ocean Dynamics* 58 (5) (2008) 429–440, ISSN 1616-7228.
- M. J. Berger, D. L. George, R. J. LeVeque, K. T. Mandli, The GeoClaw software
 for depth-averaged flows with adaptive refinement, *Adv. Water Res.* 34 (2011)
 1195–1206.
- J. Borrero, K. Sieh, M. Chlieh, C. E. Synolakis, Tsunami inundation modeling
 335 for western Sumatra, roceedings of the National Academy of Sciences of the
 United States of America 103 (52) (2006) 1967319677.
- G. Kaiser, L. Scheele, A. Kortenhaus, F. Løvholt, H. Römer, S. Leschka, The
 influence of land cover roughness on the results of high resolution tsunami
 inundation modeling, *Natural Hazards and Earth System Sciences* 11 (2011)
 340 2521–2540.

- A. Hooper, J. Pietrzak, W. Simons, J. Cui, R. Riva, M. Naeije, T. A., van Scheltinga, E. Schrama, G. Stelling, S. A., Importance of horizontal seafloor motion on tsunami height for the 2011 Mw=9.0 Tohoku-Oki earthquake, *Earth and Planetary Science Letters* 361 (1) (2013) 469–479.
- 345 F. Romano, E. Trasatti, S. Lorito, C. Piromallo, A. Piatanesi, Y. Ito, D. Zhao, K. Hirata, P. Lanucara, , M. Cocco, Structural control on the Tohoku earthquake rupture process investigated by 3D FEM, tsunami and geodetic data, *Sci. Rep.* 4 (5631).
- 350 S. Glimsdal, G. Pedersen, C. Harbitz, F. Løvholt, Dispersion of tsunamis: does it really matter?, *Nat. Hazards Earth Syst. Sci.* 13 (2013) 1507–1526.
- F. Løvholt, G. Pedersen, C. B. Harbitz, S. Glimsdal, J. Kim, On the characteristics of landslide tsunamis, *Phil. Trans. Royal Soc. London A* 373 (2053), ISSN 1364-503X.
- J. Behrens, F. Dias, New computational methods in tsunami science, *Phil. Trans. Royal. Soc. London A* 373 (2053), ISSN 1364-503X.
- 355 P. A. Madsen, O. R. Sørensen, A new form of the Boussinesq equations with improved linear dispersion characteristics. Part 2. A slowly-varying bathymetry, *Coastal Engineering* 18 (3) (1992) 183–204.
- O. Nwogu, Alternative form of Boussinesq equations for nearshore wave propa-
 360 gation, *Journal of Waterway, Port, Coastal, and Ocean Engineering* .
- D. H. Peregrine, Long waves on a beach, *Journal of Fluid Mechanics* 27 (04) (1967) 815–827.
- A. B. Kennedy, Q. Chen, J. T. Kirby, R. A. Dalrymple, Boussinesq modeling of wave transformation, breaking, and run-up. Part I: 1D., *J. Waterw., Port, Coast., Ocean Engrg.* 126 (1) (2000) 39–47.
- 365 F. Løvholt, P. Lynett, G. K. Pedersen, Simulating run-up on steep slopes with operational Boussinesq models; capabilities, spurious effects and instabilities, *Nonlin. Processes Geophys.* 20 (2013) 379–395.

- 370 P. J. Lynett, Nearshore wave modeling with high-order Boussinesq-type equations, *Journal of Waterway, Port, Coastal, and Ocean Engineering* .
- M. Tissier, P. Bonneton, F. Marche, F. Chazel, D. Lannes, A new approach to handle wave breaking in fully non-linear Boussinesq models, *Coastal Engineering* 67 (2012) 54–66.
- 375 M. Matsuyama, M. Ikeno, T. Sakakiyama, T. Takeda, A study of tsunami wave fission in an undistorted experiment, *Pure and Applied Geophysics* 164 (2-3) (2007) 617–631.
- K. Erduran, S. Ilic, V. Kutija, Hybrid finite-volume finite-difference scheme for the solution of Boussinesq equations, *Int. J. for Num. Meth. in Fluids* 49 (2005) 1213–1232.
- 380 D.-H. Kim, P. Lynett, S. Socolofsky, A depth-integrated model for weakly dispersive, turbulent, and rotational flows, *Ocean Modelling* 27 (2009) 198–214.
- F. Shi, J. T. Kirby, J. C. Harris, J. D. Geiman, S. T. Grilli, A high-order adaptive time-stepping TVD solver for Boussinesq modeling of breaking waves and coastal inundation, *Ocean Modelling* 43 (2012) 36–51.
- 385 M. Tonelli, M. Petti, Hybrid finite volume–finite difference scheme for 2DH improved Boussinesq equations, *Coastal Engineering* 56 (5) (2009) 609–620.
- P. J. Lynett, T.-R. Wu, P. L.-F. Liu, Modeling wave runup with depth-integrated equations, *Coastal Engineering* 46 (2) (2002) 89–107.
- 390 G. Wei, J. T. Kirby, Time-dependent numerical code for extended Boussinesq equations, *Journal of Waterway, Port, Coastal, and Ocean Engineering* 121 (5) (1995) 251–261.
- Clawpack Development Team, Clawpack software, URL <http://www.clawpack.org>, version 5.3.1, 2016.
- 395 R. J. LeVeque, Wave propagation algorithms for multidimensional hyperbolic systems, *Journal of Computational Physics* 131 (2) (1997) 327–353.

- D. L. George, Augmented Riemann solvers for the shallow water equations over variable topography with steady states and inundation, *Journal of Computational Physics* 227 (6) (2008) 3089–3113.
- M. Tissier, P. Bonneton, F. Marche, F. Chazel, D. Lannes, Serre Green-Naghdi
400 modelling of wave transformation breaking and run-up using a high-order finite-volume finite-difference scheme, *Coastal Engineering Proceedings* 1 (32) (2011) 13.
- D. Dutykh, T. Katsaounis, D. Mitsotakis, Finite volume methods for unidirectional dispersive wave models, *International Journal for Numerical Methods*
405 in Fluids 71 (6) (2013) 717–736.
- R. J. LeVeque, Finite volume methods for hyperbolic problems, vol. 31, Cambridge university press, 2002.
- F. Løvholt, G. Pedersen, G. Gisler, Oceanic propagation of a potential tsunami from the La Palma Island, *J. Geophys. Res.* 113 (2008) C09026, doi:10.1029.
- Q. Chen, Fully nonlinear Boussinesq-type equations for waves and currents over
410 porous beds, *J. of Eng. Mech., ASCE* 132 (2) (2006) 220–230.
- G. Wei, J. T. Kirby, S. T. Grilli, R. Subramanya, A fully nonlinear Boussinesq model for surface waves. Part 1. Highly nonlinear unsteady waves, *J. Fluid Mech.* 294 (1995) 71–92.
- P. A. Madsen, O. Sørensen, H. Schäffer, Surf zone dynamics simulated by a
415 Boussinesq type model. Part I. Model description and cross-shore motion of regular waves, *Coastal Engineering* 32 (4) (1997) 255–287.
- M. Briggs, C. Synolakis, U. Kanoglu, D. Green, Runup of solitary waves on a vertical wall, *Costal Hydraulics Laboratory*, URL <http://chl.erd.c.usace.army.mil/chl.aspx?p=s&a=Projects;36>, 1995.
420
- C. E. Synolakis, The runup of solitary waves, *Journal of Fluid Mechanics* 185 (1987) 523–545.

425 F. Løvholt, G. Pedersen, S. Glimsdal, Coupling of Dispersive Tsunami Propagation and Shallow Water Coastal, Open Oceanography Journal 4 (2010) 71–82.

C. Su, C. Gardner, Korteweg-de Vries Equation and Generalizations. III. Derivation of the Korteweg-de Vries Equation and Burgers Equation, Journal of Mathematical Physics 10 (3) (1969) 536–539.

430 T. B. Benjamin, J. L. Bona, J. J. Mahony, Model equations for long waves in nonlinear dispersive systems, Philosophical Transactions of the Royal Society of London A: Mathematical, Physical and Engineering Sciences 272 (1220) (1972) 47–78.

Appendix A. Comparison of the Boussinesq equations

A class of the Boussinesq-type equations can be written in the following form,

$$(H)_t + (Hu)_x = 0, \quad (\text{A.1})$$

$$(Hu)_t + \left(Hu^2 + \frac{gH}{2} \right)_x + gHh_x + \psi = 0, \quad (\text{A.2})$$

where ψ represents dispersion terms. If

$$\psi = \frac{Hh^2}{6}u_{xxt} - \frac{Hh}{2}(hu)_{xxt}, \quad (\text{A.3})$$

then these are called the Peregrine’s equations.

We claim that the Boussinesq equations by Schäffer et al. (1993) can be approximately reduced to the Peregrine’s form when $B = 0$. Since $H = h + \eta$,

the dispersion terms of Schäffer and Madsen with $B = 0$, can be written as,

$$\begin{aligned}
\psi &= \frac{1}{6}h^3 \left(\frac{Hu}{h} \right)_{xxt} - \frac{1}{2}h^2(Hu)_{xxt} \\
&= \frac{1}{6}h^3 u_{xxt} + \frac{1}{6}h^3 \left(\frac{\eta u}{h} \right)_{xxt} - \frac{1}{2}h^2(hu)_{xxt} - \frac{1}{2}h^2(\eta u)_{xxt} \\
&= \frac{Hh^2}{6}u_{xxt} - \frac{Hh}{2}(hu)_{xxt} \\
&\quad - \frac{\eta h^2}{6}u_{xxt} + \frac{h^3}{6} \left(\frac{\eta u}{h} \right)_{xxt} + \frac{\eta h}{2}(hu)_{xxt} - \frac{h^2}{2}(\eta u)_{xxt} \quad (\text{A.4}) \\
&= \frac{Hh^2}{6}u_{xxt} - \frac{Hh}{2}(hu)_{xxt} + \mathcal{O}(\epsilon).
\end{aligned}$$

435 Because the last four terms in (A.4) are $\mathcal{O}(\epsilon)$, the dispersion terms of Schäffer and Madsen are approximately same as the Peregrine's. However, due to the higher order terms in (A.4), Schäffer and Madsen's wave model has lower peak near the wave break than the Peregrine's model.

Now we will study the connection between Schäffer and Madsen's equations and Serre's equations. Use $H = h + \eta$ and $\eta_t = H_t = -(Hu)_x$, and assume η_{xx} is small. The dispersion terms of Schäffer and Madsen can be rewritten in a different form,

$$\begin{aligned}
\psi &= \frac{1}{6}h^3 \left(\frac{Hu}{h} \right)_{xxt} - \frac{1}{2}h^2(Hu)_{xxt} \\
&= -Hhh_x u_{xt} - \frac{1}{3}Hh^2 u_{xxt} - Hh\eta_x u_{xt} \\
&\quad - \frac{1}{6}Hh\eta u_{xxt} + \frac{1}{6}h\eta^2 u_{xxt} + h\eta(h + \eta)_x u_{xt} + \frac{1}{6}h^3 \left(\frac{\eta u}{h} \right)_{xxt}
\end{aligned}$$

Meanwhile

$$\begin{aligned}
\left(\frac{\eta u}{h} \right)_{xxt} &= -\frac{2h_x}{h^2}\eta u_{xt} + \frac{2}{h}\eta_x u_{xt} + \frac{1}{h}\eta u_{xxt} + \frac{2h_x}{h^2}(Hu)_x u_x \\
&\quad - \frac{2}{h}(Hu)_{xx} u_x - \frac{1}{h}(Hu)_x u_{xx}.
\end{aligned}$$

Therefore ψ reduces to

$$\begin{aligned}
\psi &= Hh\eta_x u_{xt} + \left(\frac{2}{3}h_x\eta - \frac{2}{3}h\eta_x \right) hu_{xt} \\
&\quad + \frac{1}{6}h^3 \left(\frac{2h_x}{h^2}(Hu)_x u_x - \frac{2}{h}(Hu)_{xx}u_x - \frac{1}{h}(Hu)_x u_{xx} \right) \\
&= -Hhh_x u_{xt} - \frac{1}{3}Hh^2 u_{xxt} + \left(\frac{2}{3}h_x\eta - \frac{2}{3}h\eta_x \right) hu_{xt} \\
&\quad + \frac{1}{6}h^3 \left(\frac{2h_x}{h^2}(Hu)_x u_x - \frac{2}{h}(Hu)_{xx}u_x - \frac{1}{h}(Hu)_x u_{xx} \right)
\end{aligned}$$

Now consider the last term

$$\begin{aligned}
&\frac{1}{6}h^3 \left(\frac{2h_x}{h^2}(Hu)_x u_x - \frac{2}{h}(Hu)_{xx}u_x - \frac{1}{h}(Hu)_x u_{xx} \right) \\
&= \frac{1}{3}h \left(h_x(Hu)_x u_x - h(Hu)_{xx}u_x - \frac{h}{2}(Hu)_x u_{xx} \right) \\
&= \frac{1}{3}h \left(h_x(H_x u + H u_x) u_x - h(2H_x u_x + H u_{xx}) u_x - \frac{h}{2}(H_x u + H u_x) u_{xx} \right) \\
&= \frac{1}{3}h \left(h_x H (u_x)^2 - 2H_x h (u_x)^2 - H h u_x u_{xx} - \frac{h}{2}H_x u u_{xx} - \frac{h}{2}H u_x u_{xx} \right) \\
&= \frac{1}{3}h \left((h_x H - 2H_x h) (u_x)^2 - \frac{3Hh}{2}u_x u_{xx} - \frac{h}{2}H_x u u_{xx} \right)
\end{aligned}$$

If we rearrange (5) and assume that $h_x\eta$, h_{xx} and η_{xx} are small, then the Madsen's dispersion terms can be written as

$$\psi \approx -Hhh_x u_{xt} - \frac{Hh^2}{3}u_{xxt} - Hh\eta_x u_{xt} - \frac{1}{6}Hh\eta u_{xxt} + \frac{1}{6}h^3 \left(\frac{\eta u}{h} \right)_{xxt}.$$

Since $\eta_t = -(Hu)_x$, we have

$$\left(\frac{\eta u}{h} \right)_{xxt} \approx \frac{2\eta_x}{h}u_{xt} + \frac{\eta}{h}u_{xxt} + \frac{2h_x}{h^2}(Hu)_x u_x - \frac{2}{h}(Hu)_{xx}u_x - \frac{1}{h}(Hu)_x u_{xx}.$$

Plugging in and dropping small terms yields to

$$\begin{aligned}
\psi &\approx -Hhh_x u_{xt} - \frac{Hh^2}{3}u_{xxt} - Hh\eta_x u_{xt} - \frac{1}{6}Hh\eta u_{xxt} \\
&\quad + \frac{h^2\eta_x}{3}u_{xt} + \frac{h^2\eta}{6}u_{xxt} + \frac{hh_x}{3}(Hu)_x u_x - \frac{h^2}{3}(Hu)_{xx}u_x - \frac{h^2}{6}(Hu)_x u_{xx} \\
&\approx -Hhh_x u_{xt} - \frac{Hh^2}{3}u_{xxt} - Hh\eta_x u_{xt} \\
&\quad + \frac{h^2\eta_x}{3}u_{xt} + \frac{hh_x}{3}(Hu)_x u_x - \frac{h^2}{3}(Hu)_{xx}u_x - \frac{h^2}{6}(Hu)_x u_{xx}. \tag{A.5}
\end{aligned}$$

The Serre's equations of (Su and Gardner, 1969) has the following dispersion terms,

$$\begin{aligned} \psi = & -Hhh_x u_{xt} - \frac{Hh^2}{3} u_{xxt} - Hh\eta_x u_{xt} \\ & - \frac{2}{3} Hh\eta u_{xxt} + \frac{Hh^2}{3} [(u_x)^2 - uu_{xx}]_x. \end{aligned} \quad (\text{A.6})$$

It is observed that (A.5) and (A.6) share common terms. As shown in Figure 10
440 numerical results also show that Schäffer and Madsen's model is more similar to Serre's equations than Peregrine's equations.

Appendix B. Stability of the hybrid scheme

It is difficult to analyze the numerical stability for our full Boussinesq equations. To obtain some insight in the stability of the proposed hybrid numerical scheme, we thus consider a closely related, but simpler, equation, namely the linearized Benjamin-Bona-Mahony (BBM) equation (Benjamin et al. (1972))

$$u_t + cu_x = \frac{h^2}{6} u_{txx}, \quad (\text{B.1})$$

where $c = \text{sqrt}gh$. This equation describes weakly dispersive, uni-directional waves in constant depth. The equation replaces the momentum equation,
445 whereas no separate continuity equation is involved.

Following, as far as possible, the steps of section 2.1.2 we rearrange the equation (B.1) as

$$(I - D)(u_t + cu_x) + Du_x = 0, \quad (\text{B.2})$$

where $D = \frac{h^2}{6} \partial_x^2$. The first step of hybrid scheme for this equation is integration of the advection equation

$$u_t + cu_x = 0, \quad (\text{B.3})$$

by the finite volume method. Then the Runge-Kutta method is applied to,

$$(1 - D)u_t + cDu_x = 0. \quad (\text{B.4})$$

which is the counterpart to (7).

If we use the centered spatial difference approximation of $O(\Delta x^2)$ accuracy on a regular grid we may employ a standard von Neumann analysis where we calculate the growth of an harmonic mode over a single time step. Expressing the coefficients of the velocity array before the time step as $u_j = e^{i\xi j \Delta x}$ we then replace the coefficient of \mathbf{M}^q , defined in section 2.1.2, by $M_j^q = U_j^q = g_q e^{i\xi j \Delta x}$, where q is 1, 2, 3, 4 or +. Correspondingly, the coefficients of the \mathbf{S}^k array, which contains auxiliary, nodal values for u_t , is expressed $(S_j^k) = s^k e^{i\xi j \Delta x}$.

The stability of the first step, (B.3), is assured by the standard CFL criterion

$$\frac{c\Delta t}{\Delta x} < 1.$$

If we instead solve the NLSW equations, as in BoussClaw, c must be replaced by the nonlinear characteristic velocity, which may lead to a more strict criterion. However, the method employed in the first step is not suited for a von Neumann stability analysis and we thus apply this technique to the second step only. Hence, we may put g_1 to unity, but it is preferable to retain it in the calculations. The Runge-Kutta scheme for time stepping, (8), may now be expressed as

$$g^2 = g^1 + \frac{\Delta t}{2} s^1, \quad g^3 = g^1 + \frac{\Delta t}{2} s^2, \quad g^4 = g^3 + \Delta t s^3, \quad (\text{B.5})$$

The discrete version of (B.4), which is the counterpart to (9) for the BBM equation reads

$$S_j^k - \frac{h^2}{6} \frac{S_{j+1}^k - 2S_j^k + S_{j-1}^k}{\Delta x^2} = -\frac{ch^2}{6} \frac{U_{j+2}^k - 2U_{j+1}^k + 2U_{j-1}^k - U_{j-2}^k}{2\Delta x^3},$$

which, inserted the harmonic expressions, implies

$$s^k = i \frac{\gamma}{\Delta t} g^k, \quad \gamma = c\Delta t \frac{2 \sin(\xi \Delta x)(1 - \cos(\xi \Delta x))}{6\Delta x^3 h^{-2} + 2\Delta x(1 - \cos(\xi \Delta x))}, \quad (\text{B.6})$$

where the Δt factors are included for convenience. The assembling of the intermediate values in the Runge-Kutta procedure, (10), now yields

$$g^+ = g^1 + \frac{\Delta t}{6} [s^1 + 2s^2 + 2s^3 + s^4]. \quad (\text{B.7})$$

By combination of (B.5) and (B.6) s^k and g^k , $k = 1..4$ can be calculated successively and combined in (B.7) to provide the value of g^+ ,

$$\begin{aligned} g^+(\gamma) &= \left(1 - \frac{1}{2}\gamma^2 + \frac{\gamma^4}{24} + \left(\frac{\gamma^3}{6} - \gamma\right)i\right) g^1 \\ |g^+(\gamma)|^2 &= \left(1 + \frac{1}{4}\gamma^4 + \frac{\gamma^8}{24^2} - \gamma^2 + \frac{\gamma^4}{12} - \frac{\gamma^6}{24} + \gamma^2 + \frac{\gamma^6}{36} - \frac{\gamma^4}{3}\right) |g^1|^2 \\ &= \left(1 - \frac{1}{72}\gamma^6 + \frac{1}{576}\gamma^8\right) |g^1|^2. \end{aligned}$$

Stability requires $|g^+(\gamma)/g^1| < 1$ which is equivalent to $|\gamma| < 2\sqrt{2}$. Moreover, it is easily seen that $\gamma < c\Delta t/\Delta x$. Hence, a sufficient condition for stability of the second step of the hybrid scheme is

$$\frac{c\Delta t}{\Delta x} < 2\sqrt{2}.$$

This is more relaxed than the CFL condition for the advection equation (B.3).

455 Therefore, if the CFL condition is satisfied in the advection equation, the fractional step is always stable with the suggested numerical scheme.

Appendix C. Energy estimates and dissipation

Appendix C.1. Velocity field

To derive the energy estimates for the Boussinesq-type equations, we define the depth-averaged velocity as,

$$\bar{u} = \frac{1}{H} \int_{-h}^{\epsilon\eta} u dz.$$

Then the velocity u can be expressed as $u = \bar{u} + \mu^2 u_1$ where

$$\int_{-h}^{\epsilon\eta} u_1 dz = 0. \tag{C.1}$$

Then the kinematic boundary condition at the bottom and zero divergence implies

$$w = -h_x u - \bar{u}_x(z+h) + O(\mu^2).$$

Appendix C.2. Energy integrals

The potential energy density per horizontal area is

$$V = \int_{-h}^{\epsilon\eta} gz dz = \frac{1}{2}\epsilon^2 g\eta^2 - \frac{1}{2}gh^2,$$

where the last term $\frac{1}{2}gh^2$ is the equilibrium energy. The kinematic energy density has two contributions,

$$T = T_u + T_w; \quad T_u = \frac{1}{2}\epsilon^2 \int_{-h}^{\epsilon\eta} u^2 dz, \quad T_w = \frac{1}{2}\epsilon^2 \mu^2 \int_{-h}^{\epsilon\eta} w^2 dz.$$

For the horizontal part, T_u is

$$T_u = \frac{1}{2}\epsilon^2 \int_{-h}^{\epsilon\eta} u^2 dz = \frac{1}{2}\epsilon^2 \int_{-h}^{\epsilon\eta} \bar{u}^2 + 2\mu^2 \bar{u}u_2 + \mu^4 u_1^2 dz = \frac{1}{2}\epsilon^2 H \bar{u}^2 + O(\epsilon^2 \mu^4),$$

since \bar{u} is independent of z and by (C.1). Assuming $\frac{1}{H} \int_{-h}^{\epsilon\eta} u^2 dz = \bar{u}^2$, the vertical part is

$$\begin{aligned} T_u &= \frac{1}{2}\epsilon^2 \mu^2 \int_{-h}^{\epsilon\eta} h_x^2 u^2 + 2h_x u \bar{u}_x (z+h) + \bar{u}_x^2 (z+h)^2 dz + O(\epsilon^2 \mu^4) \\ &= \frac{1}{2}\epsilon^2 \mu^2 H \left(h_x^2 \bar{u}^2 + H h_x \bar{u} \bar{u}_x + \frac{1}{3} H^2 \bar{u}_x^2 \right) + O(\epsilon^2 \mu^4). \end{aligned}$$

Thus the energy of a wave can be approximated as

$$E = \epsilon^2 (E_0 + \mu^2 E_1 + O(\mu^4))$$

where

$$\begin{aligned} E_0 &= \frac{1}{2} (g\eta^2 + H \bar{u}^2), \\ E_1 &= \frac{1}{6} H^3 \bar{u}_x^2 + \frac{1}{2} H^2 h_x \bar{u} \bar{u}_x + \frac{1}{2} H h_x^2 \bar{u}^2. \end{aligned}$$